CHAPTER 3

Experimental setup and Computational method

This chapter presents a detailed discussion of the three-dimensional wall jet experimental setup facility and computational methods. The wall jet experimental setup facility with different test sections is described. The test conditions and the measurement methods are discussed. This chapter also includes the validation of the experimental setup for fluid flow and heat transfer characteristics with the results available in the literature. After describing the experimental setup, the different turbulence models are presented. The details of the governing equations for the three-dimensional wall jet with the used boundary conditions are described.

3.1 Experimental details

The fluid flow characteristics are tested for the different initial and boundary conditions in different geometries of the test section. In the first stage, the effect of the initial condition is tested inside the sidewall enclosure. The initial condition of the jet is varied by changing the nozzle length. In the second stage, the experimental facility is devised to study the effect of sidewall enclosure. Further, the final experiment is conducted for the different widths of the sidewall enclosure for fluid flow and heat transfer characteristics.

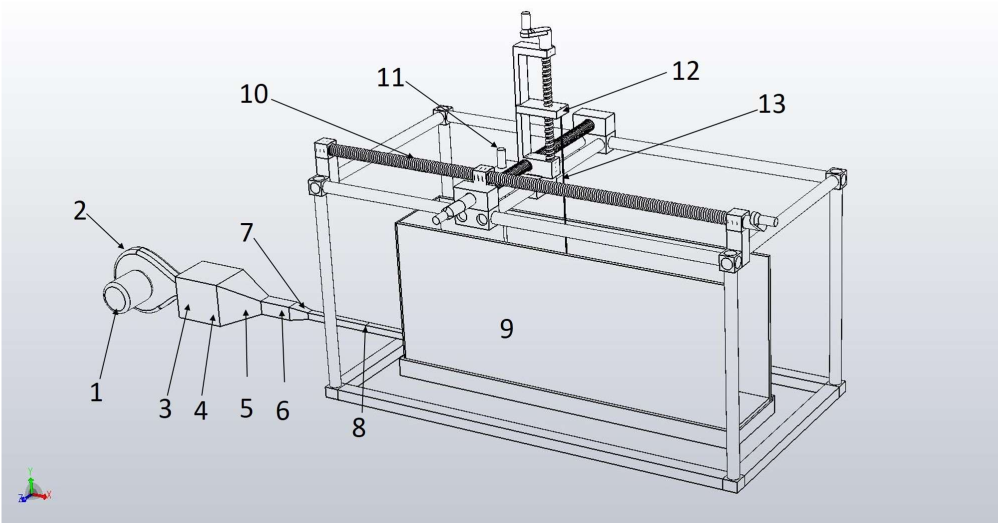

Figure 3.1: Schematic of the experimental setup (1. Air blower, 2. Air filter, 3. Flow stabilizer, 4. Heater, 5. Reducer duct 1, 6. Flow straightener, 7. Reducer duct 2, 8. Square nozzle, 9. Test section, 10. Transversing mechanism for anemometer, 11. Anemometer, 12. Transversing mechanism for thermocouple, 13. Thermocouple)

3.1.1 Wall jet facility

The present experimental setup is made to conduct the fluid flow and heat transfer characteristics of the three-dimensional turbulent wall jet. A schematic diagram of the experimental setup is shown in Figure 3.1. A Ralliwolf make (Power 350 W and discharge 1.5 m^3/min) centrifugal air blower is used to supply the air at a constant bulk velocity. The blower is connected with a single-phase variac to control the velocity of the air. The blower is mounted over a base to remove the machine vibration. The air is supplied to the flow stabilizer from the air blower to settle down the foreign particles. Then, it is sent to a flow straightener to remove eddies and swirl from the flow stream. The length of the flow straightener is kept greater than 10 d_t, where d_t is the diameter of the embedded straightener pipe. Therefore, the length of the flow straightener is chosen 60 mm, with 3 mm embedded pipe diameter. A low reduction ratio of the reducer duct is used for joining from the exit of the flow straightener to the entry of the square nozzle. Now, the square nozzle is supplied the air inside the test section. The cross-section of the square nozzle is $20 \pm 0.5 mm \times 20 \pm 0.5 mm$.

For the heated wall jet facility, a mesh of electric heater is employed inside the flow stabilizer. A single-phase variac controls the heater. All the components which are associated with heated air encounter different type of heat losses. These heat losses may lead to change in the surrounding condition, and may change the initial condition and

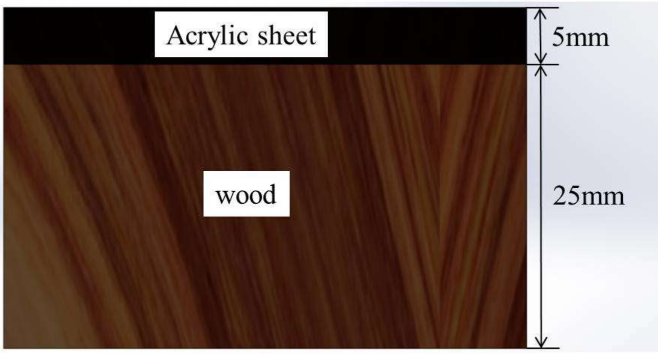

Figure 3.2: Adiabatic surface

temperature profile at the jet exit. In order to minimize these losses, all the components are insulated with thick insulation strip of asbestos. The bottom wall of the test section is made from $5mm$ thick acrylic sheet. The acrylic sheet is chosen for its low thermal conductivity to make the surface adiabatic. Below the acrylic sheet, a $25mm$ thick wood base is placed for the insulation (Figure 3.2).

3.1.2 Measurement procedure

The mean velocity fields inside the test section are measured with a hot wire anemometer probe. A three-dimensional transversal mechanism supports the hot wire anemometer probe to measure the velocity at different locations of the test sections. The anemometer probe is calibrated in an air standard facility for free jet for the velocity range $0\, m/sec$ to $50\, m/sec$ with a 95.45% confidence level with a coverage factor of k=2. The velocity of air at the jet exit is determined by calculating the pressure drop. After calibrating the hotwire, the velocity is measured by the anemometer for the free jet and compared with the another calibrated hotwire anemometer. The accuracy and resolution of the hotwire anemometer are ±0.03 m/s and 0.01 m/s, respectively. The different sample sizes are used for different locations (i.e. near the wall or away from the wall) to get the 95% confidence level.

The temperature fields inside the test section are measured with a fine wire thermocouple probe. The thermocouple probe is made from $0.13mm$ diameter of K-type thermocouple wire. The bead diameter of the spherical junction probe is $0.4mm$. The thermocouple wire is wrapped across the very thin structure support. The thermocouple bead is placed slightly below the structural support to reduce heat losses due to any contact of structural support. The thermocouple is calibrated (in a calibrator) to measure the air temperature in the flow domain. This thermocouple probe structure is moved inside the flow field with the help of a transversal mechanism. The minimum resolution of the

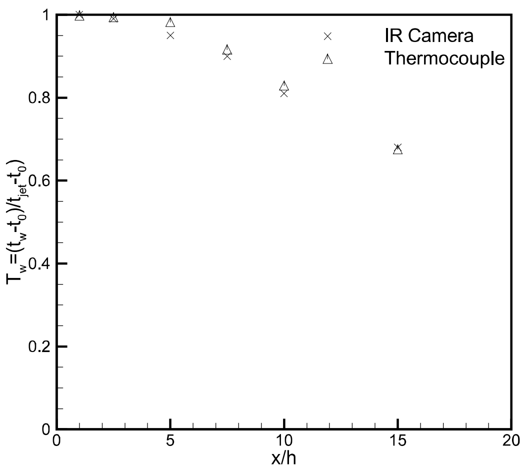

Figure 3.3: Centerline surface temperature decay

transversing mechanism is $\pm 0.5 mm$. The thermocouple data are recorded with the NI 9213 data acquisition system. In the present work, a frequency (f_c) of 200Hz and the data sampling rates (f_s) of 1000 are chosen.

The thermal imaging infrared camera is used to measure the temperature over the bottom wall surface. The infrared camera is FLIR make with a model number E75. The infrared thermal imaging camera is calibrated outside the laboratory. A camera holding mechanism is attached above the bottom wall. The thermal imaging IR camera is used to capture the image from 1 m above the bottom wall. The IR image contains 640 × 480 pixels. The temperature resolution of the IR is 0.1 ^0C . The temperature range of the camera is selected as $-20\ ^0C$ to $120\ ^0C$. The captured image is processed in FLIR thermal image tool software to analyze the surface temperature. The maximum variation of temperature measured by a thermocouple and FLIR IR camera is 0.2^0C . The bottom wall surface is painted with matte-black paint for higher emissivity. The average emmisivity of the bottom wall is found as 0.98. The centerline bottom wall temperature below the jet is measured with IR thermal imaging camera and thermocouple as shown in Figure 3.3. The Figure indicates that both the techniques provide the same temperature profile.

The test section is placed in the ambient condition. The fluid flow characteristics are measured for the unheated jet, whereas the heat transfer characteristics are measured for the different jet exit temperatures with respect to the ambient temperature. The ambient temperature conditions are monitored during the experimental run.

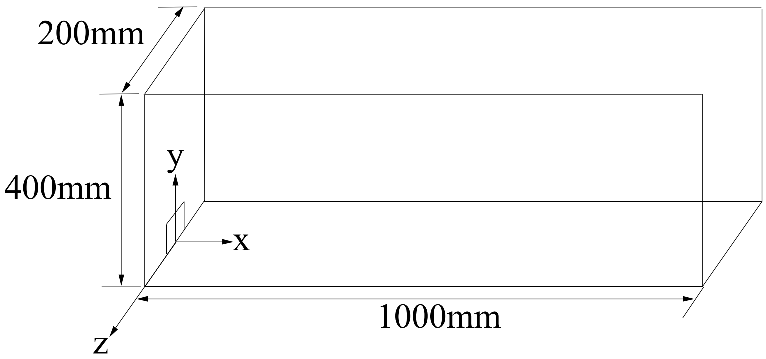

Figure 3.4: Schematic of the test section of initial conditions with Cartesian coordinate

3.1.3 Description of experimental test sections and experimental test conditions with jet inlet profiles

Three different test sections are made to test the different initial and boundary conditions, as mentioned in the objective of chapter 1 of the present study.

3.1.3.1 Effect of initial conditions

The different initial conditions are generated by changing the length of the square nozzle ($20 \pm 0.5mm\times$ $20\pm0.5mm$). The length of the square nozzle is changed as $200mm$, $1000mm$, and $1800mm$. The test section of the experimental setup is made of a clear acrylic sheet having dimensions 1000mm long, 200mm wide, as shown in Figure 3.4. A $200mm \times 400mm$ vertical wall is placed at the nozzle exit plane in order to restrict the entrainment behind the nozzle. Two parallel plates of $400mm \times 1000mm$ are placed at the lateral positions of $\pm100mm$ from the vertical jet centerline plane, termed as sidewalls. The Cartesian coordinate is assumed as shown in Figure 3.4; $x = 0$ is at the nozzle exit, $y = 0$ is at the flat surface wall and $z = 0$ is at the mid plane of the nozzle. The air stream is blown through the square nozzle in the test section to form a three-dimensional turbulent wall jet.

The jet exit velocity profile for the nozzle length $200mm$, $1000mm$, and $1800mm$ are shown in Figure 3.5. All these velocity profiles are developing in nature having a constant bulk mean velocity(=20.3 m/s). The jet exit velocity profiles are normalised by the corresponding jet exit velocity $\left(u_{jet}\right)$ of the different nozzles. The Reynolds number (Re) based on the bulk mean velocity (u_b) and nozzle height (h) is 25,000 for all the nozzles.

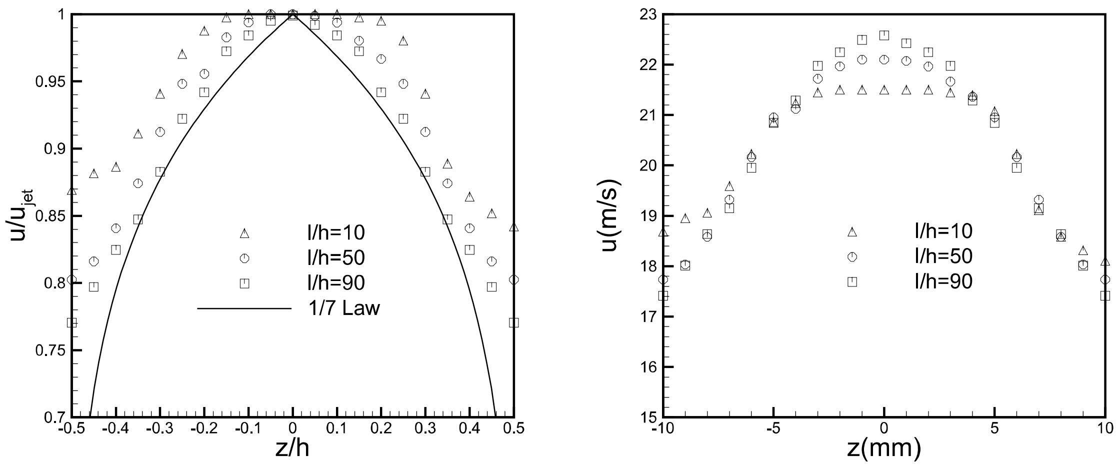

(a) (b)

Figure 3.5: Jet exit velocity profiles for different nozzle length (a) Non-dimensional jet exit velocity profile, and (b) Dimensional jet exit velocity profile

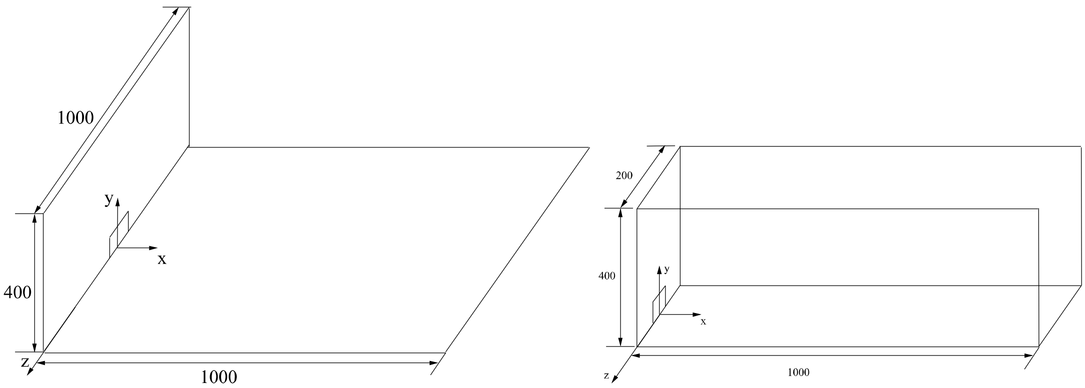

(a) (b)

Figure 3.6: Schematic of the test section of with and without sidewalls with cartesian coordinate

3.1.3.2 Effect of sidewalls

A schematic diagram of the test sections is shown in Figure 3.6. For the fluid flow and thermal behaviour of the wall jet, two different configurations of the test section are created, i.e. without sidewall across the jet centerline termed as configuration 1 (Figure 3.6a), and with sidewall across the jet centerline termed as configuration 2 (Figure 3.6b). Configuration 1 has a backwall ($1000mm \times 400mm$) at the jet exit plane, whereas no sidewall is present at the lateral locations. The bottom wall has the dimension of $1000mm \times 1000mm$ for configuration 1. Configuration 2 is similar to the Configuration 1 but it has two sidewalls at the lateral locations of $\pm 100mm$ from the vertical jet centerline plane. The bottom wall has the dimension of $1000mm \times 200mm$ for configuration 2. The sidewalls across the jet centerline are also made from the acrylic sheet for maintaining the adiabatic conditions.

A developing velocity profile generated by a square nozzle (length=$200mm$) is considered for this work. The ratio of bulk mean velocity (u_b) to jet exit velocity (u_{jet}) suggests that the generated velocity profile is neither flat nor fully developed. It should be noted here that the jet exit velocity profile is not top hat velocity profile as seen in contoured nozzles [4, 55]. The jet exit Reynolds number based on the bulk mean velocity ($u_b = 20.3m/s$) and nozzle height ($h = 20 \pm 0.5mm$) is 25000 for both the configurations.

The thermal characteristics of the three-dimensional wall jet is also measured. In this work, the heated jet characteristics are measured for the same jet exit Reynolds number as used during the measurement of fluid flow characteristics. The thermal characteristics of the three-dimensional turbulent heated wall jets are measured for two different jet exit temperatures $\left(t_{jet}\right)$, 20^0C and 40^0C. The effect of buoyancy is also checked at the exit of the nozzle. For this, the ratio of the buoyancy to inertia force $\left(Gr_h/Re_h^2\right)$ is calculated. The estimated value is found in the order of 10^{-5} for all the cases, so the effect of buoyancy is neglected.

The non dimensional temperature and mean velocity profile at the nozzle exit are plotted for a Reynolds number of 25000, as shown in Figure 3.7.The jet exit velocity profile is normalised by the maximum jet exit velocity $\left(u_{jet}\right)$, whereas temperature profile are normalised by the jet exit temperature above the ambient condition $\left(t_{jet} - t_o\right)$. Since jet is produced using a 200 mm long square nozzle, the profile is neither flat nor following 1/7 law. For the comparison purpose, 1/7 profile is also plotted in Figure 3.7. The jet exit temperature fluctuation profile is also shown in Figure 3.8. From the Figure 3.8, it can be seen that the temperature fluctuation at the jet exit is approximately uniform.

3.1.3.3 Effect of sidewall width

The effect of sidewall on the three-dimensional turbulent wall jet is characterised by the four different widths (W= $140mm$, $160mm$, $180mm$ and $200mm$) of the sidewall enclosures (SWEs). The test section of SWE is made from $5mm$ thick acrylic sheet. The sidewalls (length of $1000mm$ and height of $400mm$) are placed at the lateral locations of $\pm 70mm$, $\pm 80mm$, $\pm 90mm$ and $\pm 100mm$ from the vertical jet centerline plane to make the different width of SWEs (Figure 3.9). The bottom wall surface ($1000mm \times Wmm$) is also made from a 5mm thick acrylic sheet, W is the width of SWE. The width (W) of the SWE is varied as $140mm$, $160mm$, $180mm$, and $200mm$. The acrylic sheet with a low thermal conductivity

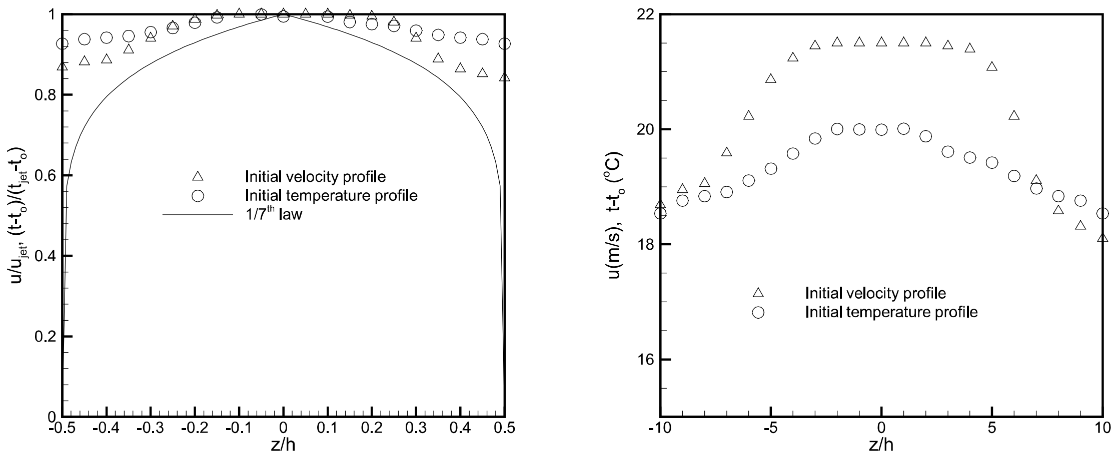

(a) (b)

Figure 3.7: Initial jet profiles of with and without sidewalls conditions (a) Non-dimensional jet exit profiles, (b) Dimensional jet exit profiles for 200mm nozzle

makes the bottom wall surface adiabatic. Below the acrylic sheet, the bottom wall is insulated with a $25mm$ thick wooden base. The coordinate system is assumed as $x = 0$ at the nozzle exit plane, $y = 0$ at the bottom wall surface plane and $z = 0$ at the symmetry plane of the nozzle exit.

For this, ambient air is blown over an adiabatic flat surface using a pipe of length 200mm with a square nozzle of cross-sectional area $20mm \times 20mm$. The fluid flow characteristics for all the SWEs are measured at a Reynolds number, $Re_h = u_b h/\nu = 25000$, where $u_b = 20.3m/s$ is the exit velocity from the jet, h is the height of the square nozzle and ν is the kinematic viscosity of the air at the room temperature. A non-dimensional mean velocity profile and dimensional velocity profiles at the nozzle exit are shown in section 3.1.3.2 of Figure 3.7 for the Reynolds number (Re) of 25,000.

3.1.4 Uncertainty analysis

The uncertainty for the primary and derived quantities is performed by the method described by Abernethy et al. [124], Coleman and Steele [125]. The total uncertainty of the measured quantities (velocity and temperature) inside the test section can be expressed as

$$\text{Uncertainty of measured quantities} = (Precision error + Bias error)^{1/2}$$

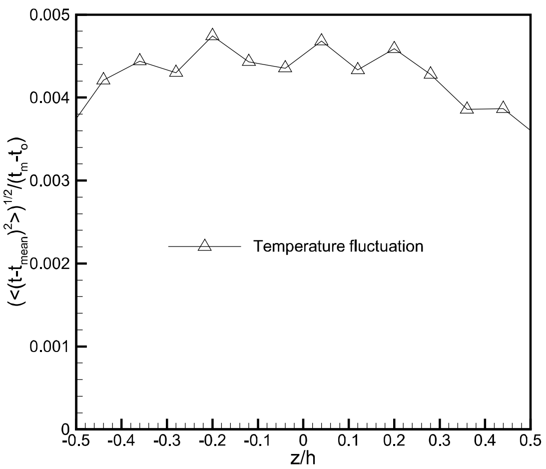

Figure 3.8: Temperature fluctuation profile at the jet exit

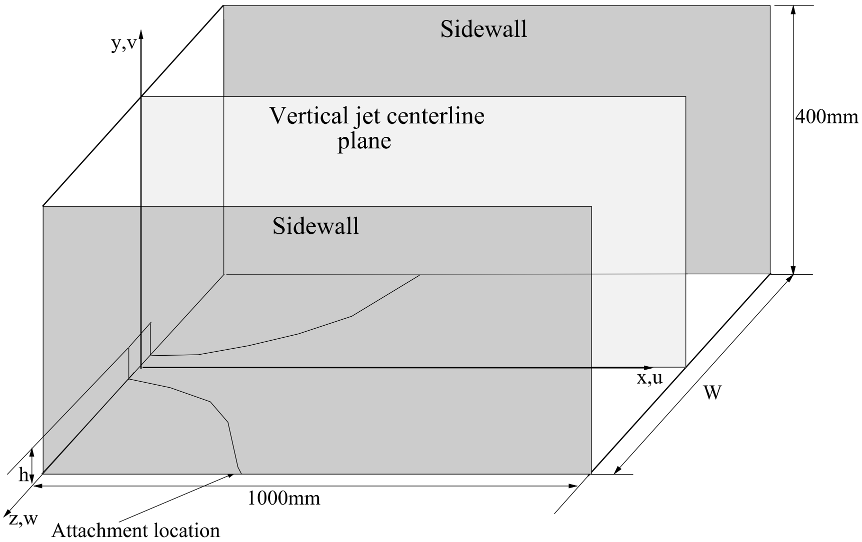

Figure 3.9: Schematic of the test section of sidewall enclosures with cartesian coordinate

The uncertainty in velocity measurement is limited by the anemometer probe's accuracy and resolution of the hot wire. Uncertainty in temperature measurement depends on the thermocouple probe's accuracy and the response time. The bias error involves the systemic error of any primary quantity. It is therefore constant for a given set of experiments with different quantities. There is a common bias error in the different sets of repeated experiments. The error of precision is calculated based on the sample size, as proposed by Abernethy et al. [124]:

$$P = \frac{\left[\sum_{i=1}^{n}(X_k - \overline{X})^2\right]^{1/2}}{N-1}$$

$$P_x = \frac{P}{\sqrt{N}}$$

Where P is the calculated quantity precision factor, N is the experiment's sample size. The error in temperature measurement may be due to the bias error, like uncertainty in calibration, or random error, like uncertainty in wire positioning, minimum step size of the transversal mechanism and the experimental repeatability. The uncertainties in measured mean temperature with IR camera and thermocouple are $\pm 0.2^0 C$ and $\pm 0.65^0 C$, respectively. The uncertainty in fluctuating temperature is measured as 1.59%. The hot wire probe is moved in the flow domain by using a transversal mechanism. The hot wire probe is calibrated in a separate facility. The hot wire anemometer probe's sensitivity is 0.03 m/s, and the anemometer probe's resolution is 0.01 m/s. During the measurement of the velocity of the unheated jet, the variation of temperature during the experiment is kept constant and it is within the tolerance limit of $\pm 1^0 C$, so no correction in velocity is incorporated. The uncertainty in the calculated Reynolds number depends on the specific quantity measured (velocity and height of the nozzle). This calculated quantity includes bias and precision errors that propagate the Reynolds and Grashof numbers accumulated errors. The uncertainty of the Reynolds number (Re) based on all the parameters is determined following Kline and McClintock [126], which is

$$\Delta Re = \pm\sqrt{\left(\frac{\Delta Re}{\partial u} \times \Delta u\right)^2 + \left(\frac{\Delta Re}{\partial h} \times \Delta h\right)^2}$$

Where ΔRe is the maximum uncertainty of the calculated Reynolds number. Table 3.1 lists the complete uncertainty of the primary and derived quantities of the experimental setup.

Table 3.1: The maximum uncertainty of the primary and derived quantities

Sl No.	Quantities	Uncertainty
1	Nozzle height	$\pm 0.5\,mm$
2	Movement of transverse mechanism in longitudinal direction	$\pm 0.5\,mm$
3	Movement of transverse mechanism in lateral direction	$\pm 0.5\,mm$
4	Movement of transverse mechanism in vertical direction	$\pm 0.5\,mm$
5	Velocity (about centerline)	$\pm 1.47\,\%$
6	Velocity (Near the sidewall)	$\pm 2.01\,\%$
7	Reynolds number	$\pm 4.00\,\%$
8	Mean temperature (Thermocouple)	$\pm 0.65^0 C$
9	IR camera	$\pm 0.2^0 C$
10	Fluctuating temperature	$\pm 1.59\%$

3.1.5 Experimental setup validation

3.1.5.1 Fluid flow validation

The experimental setup is validated with the experimental data of Hall and Ewing [9] for the decay of maximum mean velocity along the downstream direction. They have considered a square nozzle with Re= 89,600. For the validation of the experimental setup for fluid flow characteristics, the nozzle with l/h=100 is considered, and the boundary conditions are taken the same as reported in Hall and Ewing [9]. The Reynolds numbers (Re) is fixed at 80,000. We could not go beyond Re=80,000, as there was appreciable heating of the air by the blower. The decay of the maximum mean velocity profile with streamwise direction is shown in Figure 3.10. It can be noticed that the present result of Re= 80,000 matches quite well with the published experimental result of Hall and Ewing [9].

3.1.5.2 Heat transfer validation

Before measuring the heat transfer characteristics for this work, the present experimental setup is also validated for the heat transfer characteristics. The experimental setup for the heat transfer characteristics is validated with the results of Mi et al. [91]. Similar to Mi et al. [91], a free jet is constructed with the present turbulent jet facility. The boundary condition is taken same as that of Mi et al. [91] and compared the temperature decay along the jet centerline. Mi et al. [91] considered the fully developed flow (n=6.5) with jet exit Reynolds number 16,000. The jet exit temperature for the validation is considered $(t_{jet} - t_o)$ as $50K$, similar to Mi et al. [91]. From the Figure 3.11, it can be seen that the centerline temperature decay matches very well with the experimental results of Mi et al. [91].

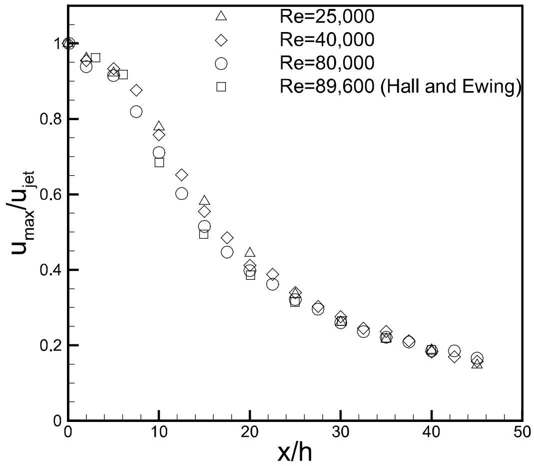

Figure 3.10: Validation of experimental setup for fluid flow characteristics

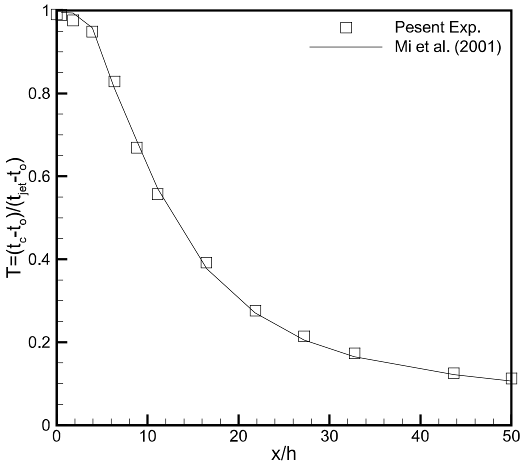

Figure 3.11: Validation of the experimental setup

3.2 Computational methods

The fluid flow and heat transfer characteristics of the turbulent wall jet for different initial and boundary conditions are modelled using Reynolds averaged Navier-Stokes (RANS) equations. The mean flow is assumed as a three-dimensional and steady for all the test conditions. The body force is assumed to be negligible for all the cases. The Boussinesq approximation is used to link the Reynolds stresses with the velocity gradients. The fluid properties are considered constant. The two different Low Reynolds number models, i.e. Yang and Shih [47] and Launder and Sharma [48], are used for the numerical simulations.

Molecular viscosity directly influences turbulent motion in the low-Reynolds number area near the viscous sub-layer zone of the flow field. Throughout the flow domain, the turbulent Reynolds number (Re_t) fluctuates. The low Reynolds number models resolve entire boundary layer region with the viscous sub-layer zone of the flow domain. The wall boundary function, damping functions (f_1, f_2 and f_μ) and additional terms (D_n and E_n) are used in the low Reynolds number turbulence model equations for their validity in the viscous sublayer region. The non-dimensional parameters and governing equations are presented below.

3.2.1 Governing equations

The non-dimensional parameters are defined as:

$$U_i = \frac{\overline{u_i}}{u_{jet}},\ X_i = \frac{x_i}{h},\ P = \frac{\overline{p} - p_0}{\rho u_{jet}^2}$$

$$k_n = \frac{k}{u_{jet}^2},\ \varepsilon_n = \frac{\varepsilon}{u_{jet}^3/h},\ \nu_{t,n} = \frac{\nu_t}{\nu}$$

$$T = \frac{t - t_o}{t_{jet} - t_o},\ Gr = \frac{g\beta t h^3}{\nu\alpha},\ \alpha_{t,n} = \frac{\nu_{t,n}}{Pr_t} \tag{3.1}$$

Now, non-dimensional equations are:

Continuity equation:

$$\frac{\partial U_i}{\partial X_i} = 0 \tag{3.2}$$

Momentum equation:

$$\bar{U_j}\frac{\partial \overline{U_i}}{\partial X_j} = -\frac{\partial}{\partial X_i}\left(\bar{P} + \frac{2}{3}k_n\right) + \frac{1}{Re}\frac{\partial}{\partial X_j}\left(1 + \nu_{t,n}\right)\left(\frac{\partial \overline{U_i}}{\partial X_j} + \frac{\partial \overline{U_j}}{\partial X_i}\right) \tag{3.3}$$

Energy equation:

$$\bar{U_j}\frac{\partial \bar{T}}{\partial X_j} = \frac{1}{Re{\cdot}Pr}\left(\frac{\partial}{\partial X_j}\left(1 + \alpha_{t,n}\right)\frac{\partial \bar{T}}{\partial X_j}\right) \tag{3.4}$$

Turbulent kinetic energy (k_n)equation:

$$\frac{\partial \bar{U_j} k_n}{\partial X_j} = \frac{1}{Re}\frac{\partial}{\partial X_j}\left(1 + \frac{\nu_{t,n}}{\sigma_k}\right)\frac{\partial k_n}{\partial X_j} + G_n - \varepsilon_n - D_n \tag{3.5}$$

Rate of dissipation (ε_n) equation:

$$\frac{\partial\left(\bar{U}_j\varepsilon_n\right)}{\partial X_j} = \frac{1}{Re}\frac{\partial}{\partial X_j}\left(1+\frac{\nu_{t,n}}{\sigma_\varepsilon}\right)\frac{\partial\varepsilon_{t,n}}{\partial X_j} + C_{1\varepsilon}f_1\frac{\varepsilon_n}{k_n}G_n - C_{2\varepsilon}f_2\frac{\varepsilon_n^2}{k_n} + E_n \tag{3.6}$$

Rate of shear production (G_n):

$$G_n = \frac{\nu_{t,n}}{Re}\left(\frac{\partial\bar{U}_i}{\partial X_j}+\frac{\partial\bar{U}_j}{\partial X_i}\right)\frac{\partial\bar{U}_i}{\partial X_j} \tag{3.7}$$

Eddy viscosity $\left(\nu_{t,n}\right)$

$$\nu_{t,n} = C_\mu f_\mu Re\frac{k_n^2}{\varepsilon_n} \tag{3.8}$$

The model functions f_1, f_2 and f_μ for LS and YS turbulence model are defined in table 3.2. Additional terms D_n and E_n, and wall boundary function for LS and YS model are defined in table 3.3. The model constants for LS and YS model are given as $\sigma_k = 1.0$, $\sigma_\varepsilon = 1.30$, $\sigma_{1\varepsilon} = 1.44$, $\sigma_{2\varepsilon} = 1.92$ and C_μ=0.09 [47, 48].

Table 3.2: Definition of model function

Model	f_μ	f_1	f_2
LS	$exp\left(\frac{-3.4}{(1+Re_t/50)^2}\right)$	1	$1-0.3\,exp\left(-Re_t^2\right)$
YS	$\left(1+\frac{1}{\sqrt{Re_t}}\right)\left(1-exp\left(-aRe_y-bRe_y^3-cRe_y^5\right)\right)^{0.5}$ $a = 1.5\times10^{-4}$, $b = 5.0\times10^{-7}$ and $c = 1\times10^{-10}$	$\left(\frac{\sqrt{Re_t}}{1+\sqrt{Re_t}}\right)$	$\left(\frac{\sqrt{Re_t}}{1+\sqrt{Re_t}}\right)$

Table 3.3: Additional terms and wall boundary condition for low Reynolds number model

Model	D_n	E_n	Wall boundary function
LS	$\frac{2}{Re}\left(\frac{\partial\sqrt{k_n}}{\partial X_j}\right)^2$	$\frac{2\nu_{t,n}}{Re^2}\left(\frac{\partial^2\overline{U_i}}{\partial X_j^2}\right)$	$\epsilon_n = 0$
YS	0	$\frac{\nu_{t,n}}{Re^2}\left(\frac{\partial^2\overline{U_i}}{\partial X_j^2}\right)$	$\epsilon_n = \frac{2}{Re}\left(\frac{\partial\sqrt{k_n}}{\partial n}\right)^2$

3.2.2 Justification of using YS and LS turbulence models

Nasr and Lai [41] compared the experimental and numerical results of the turbulent offset jet. Nasr and Lai [41] have measured the mean flow and turbulence characteristics of the turbulent offset jet with the Laser Doppler Anemometry (LDA) at a Reynolds number of 11,000 and did the numerical simulation of the problem by considering the three different turbulence models (the standard $k-\varepsilon$, Re-normalizing group model (RNG) and Reynolds stress model (RSM)). Comparing the experimental results with the numerical results obtained by different turbulence models shows that the standard $k-\varepsilon$ turbulence model is more appropriate for predicting the turbulent jets. Seyedein et al. [127] studied the flow and thermal characteristics of an impinging type turbulent jet through numerical simulation at the Reynolds number 5,000 to 20,000. Authors considered the standard $k-\varepsilon$ turbulence model and two low Reynolds number turbulence models suggested by Lam and Bremhorst and Launder and Sharma [48] and noted that the low Reynolds number turbulence model performed better as compared to the standard $k-\varepsilon$ turbulence model and Launder and Sharma [48] model shows better agreement with the experimental results. Rathore and Das [128] reproduced the results of He et al. [129] for the buoyancy opposed flow with the low Reynolds number Yang and Shih [47] turbulence model and systematically compared with the experimental results and reported quite a good match with the experimental results. El-Gabry and Kaminski [130] studied the cross-flow turbulent jet with YS [47] turbulence model. Senthooran and Parameswaran [131] showed the applicability of the Yang and Shih [47] model in natural convection flow over a flat plate. Rathore and Das [46, 132] used Yang and Shih [47] and Launder and Sharma [48] turbulence models for the wall and offset jets and reported a good match with the different experimental results.

So, for the present case, low Reynolds number Yang and Shih [47] and Launder and Sharma [48] models are used to simulate the three-dimensional wall jet for different initial and boundary conditions.

3.2.3 Computational domains and jet inlet conditions

3.2.3.1 Initial condition

The computational domain for numerical simulation is similar to the test section, as shown in section 3.1.3.1. The computational domain measures as $50h \times 10h \times 20h$, where $h = 20mm$ is the height of the square nozzle. For each case, two parallel plates (sidewall) are taken at the lateral position of $\pm 5h$ from the vertical jet centerline plane. Cartesian coordinate for the numerical simulation is assumed similar to the experimental setup, as shown in Figure 3.12.

This work investigates the effect of developing initial conditions on a 3D turbulent wall jet through experimental method and the numerical simulation. The initial conditions of the jet used for numerical simulation are defined in the section 3.1.3.1. The initial conditions of the jet are neither a fully developed ($1/7^{th}$ power law) nor a top-hat profile. The numerical analysis has been carried out for these initial conditions generated by the three

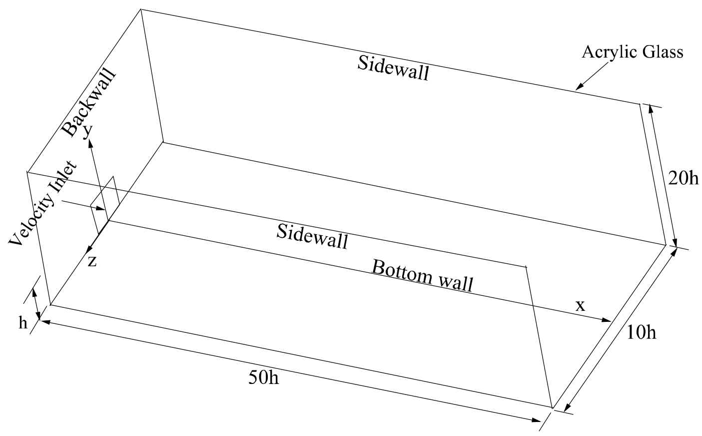

Figure 3.12: Computational domain

different nozzle lengths (l/h = 10, 50 and 90) for the present three-dimensional turbulent wall jet geometry.

3.2.3.2 With and without sidewalls

The two different computational domains are considered to characterize the sidewall effect on fluid flow and heat transfer characteristics. The non-dimensional measurement of the computational domain measures as 50 × 30 × 20 and 50 × 10 × 20 for configuration 1 and configuration 2, respectively. The computational domains for both the configurations are shown in Figure 3.13. The coordinate system for the numerical simulation is assumed similar to the experimental setup for both the configurations, as described in section 3.1.3.2. The numerical simulation for fluid flow and heat transfer characteristics is carried out at a Reynolds number of ($Re = 25,000$).

In this work, the inlet velocity and temperature profile of the jet exit are used similar to the velocity and temperature profile obtained from the experimental results, as described in section 3.1.3.2. The non-dimensional velocity and temperature profiles characterize the different turbulent characteristics of the three-dimensional wall jet.

3.2.3.3 Sidewall enclosure width

In this work, the three-dimensional turbulent wall jet in different widths of sidewall enclosures (SWEs) is numerically simulated at a Reynolds number of 25,000. The width of SWE is varied, similar to the experimental test section, as defined in section 3.1.3.3. The numerical simulation is carried out for every width (W=140mm, 160mm, 180mm, and 200mm) of the SWE. A computational domain for the different widths of SWEs is shown in Figure 3.14. Each SWEs is given a developing jet inlet velocity profile condition generated by a

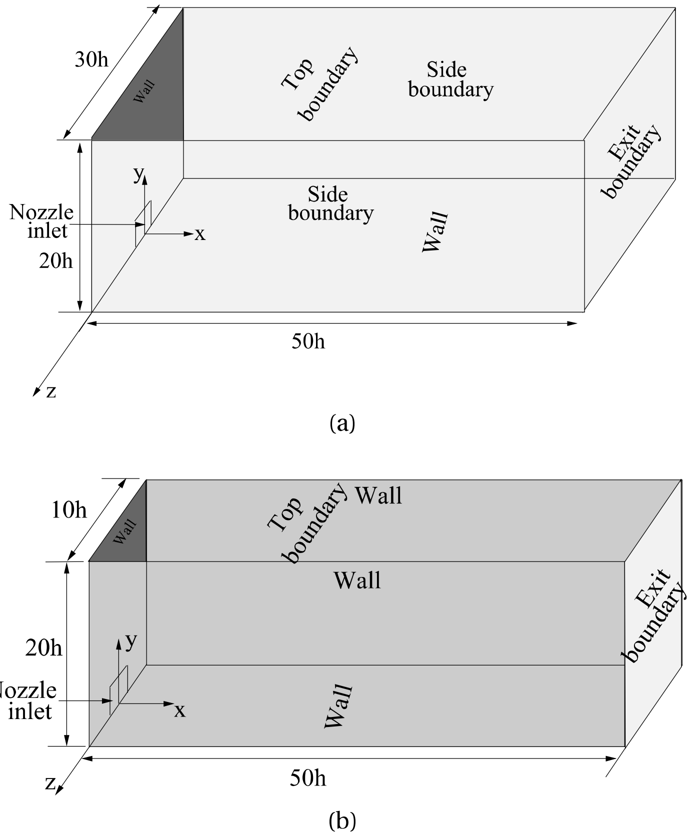

Figure 3.13: Computational domain for numerical simulation (a) Configuration 1 (b) Configuration 2

200mm square nozzle, as described in section 3.1.3.3.

3.2.4 Boundary conditions of different wall jet configurations

The non-dimensional boundary conditions applied for YS and LS turbulence models in different computational domains are as follows:

Wall jet inlet : U=1, V=0, W=0, $k_n = 1.5\, I^2$ where $I = 0.05$, $\varepsilon_n = \left(C_\mu^{3/4} k_n^{3/2}\right)/0.07$

Solid walls (bottom wall, backwall and sidewalls) : U=0, V=0, W=0, $k_n = 0$, $\varepsilon_n = 0$ (LS model) , $\varepsilon_n = \frac{2}{Re}\left(\frac{\partial\sqrt{k_n}}{\partial n}\right)^2$ (YS model)

Top inflow, side (without sidewall case) and exit boundary: $\frac{\partial \phi}{\partial n} = 0$ where $\phi = U, V, W$, k_n and ε_n.

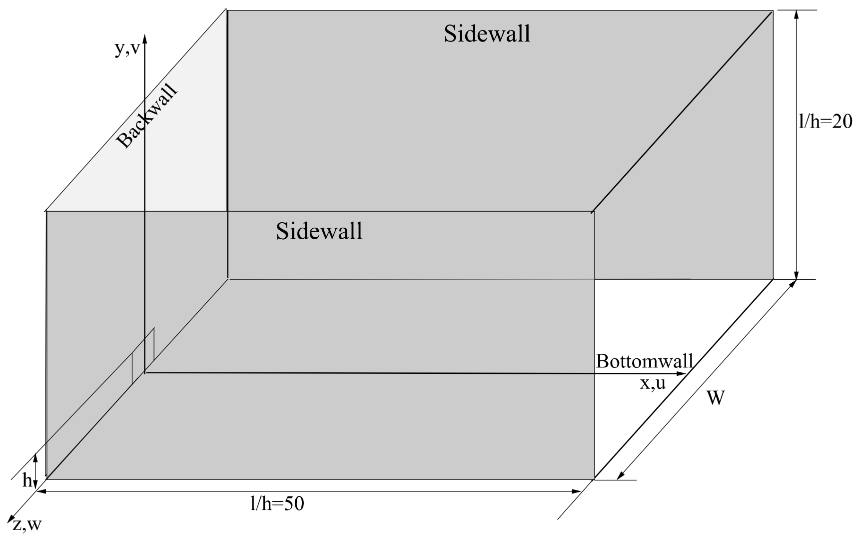

Figure 3.14: Computational domain of SWE

3.2.5 Numerical Scheme and method of Solution

The finite volume method is used to discretize the three-dimensional Reynolds averaged Navier Stokes (RANS) equations (described in section 3.2.1). The convective terms are discretized using the power-law upwind scheme. The power-law method gives a reliable result (Nasr and Lai [41]). The diffusive terms in the governing equations are discretized using the central difference scheme to ensure second-order accuracy. A detailed discretization of turbulent kinetic energy and dissipation rate equations are provided by Biswas [133], which is used in the present numerical simulations. For defining the inflow and outflow boundary conditions for the numerical simulations, $50h$ and $20h$ distances are considered in the downstream and wall-normal directions, respectively. The lateral width is changed based on the different test sections. The lateral width of the computational domain is changed as $7h$, $8h$, $9h$, $10h$, and $30h$. These distances in different directions are similar to the experimental test sections and sufficiently long to develop the flow to achieve similarity solution for fluid flow and heat transfer characteristics. The collocated grid arrangement is used on a structured grid system for the primitive variables. Finer grids are used near the wall and near the jet exit plane while grid is expanded away from the wall and the jet exit using geometrical expansion scheme $\sum = (a(1-r^n)/(1-r))$, where a is the size of the control volume, r is the expansion ratio, n is the number of grid points in different directions, and $\sum$ is the domain size. The different expansion ratios (r) are used in different directions. The velocity and pressure coupling is handled using the semi-implicit pressure linked equation (SIMPLE) method described by Patankar [134]. The under relaxation factor used for the pressure correction equation is 0.15-0.2. The algebraic differential equations are solved by the strongly implicit procedure (SIP) method suggested by Stone [135]. The numerical simulations are assumed to be converged when the residuals for each case fall below 10^{-5}

3.2.6 Validation of the numerical code and grid independence test

The numerical code of the fluid flow and heat transfer characteristics is validated with the present experimental results produces by the different test sections (described in section 3.1.3) of the wall jet. The numerical code is written in the FORTRAN language and ran on a 64bit fedora-25 platform. In the subsequent sections, the code validation and grid independence test are performed for every set of aforementioned wall jet configurations. The subsequent sections have two parts, the first part is the code validation, and the second is the grid independence test.

3.2.6.1 Effect of Initial conditions

The written numerical code is validated by comparing the numerical results obtained from YS [47] and LS [48] turbulence models with the present experimental results for similar jet inlet velocity profiles. The lateral and wall-normal velocity profiles obtained from numerical and experimental methods at the downstream locations $x/h = 2$ and 20 are compared individually for all the initial conditions. A slight deviation is observed for the mean velocity near the edge of the lateral and wall-normal velocity profiles. This deviation is due to the assumption used in the RANS numerical analysis and velocity measurement technique used to measure the velocity profiles. Figure 3.15 shows overall a good agreement of the numerical results of YS and LS turbulence models with the experimental results.

The grid independence test is carried out for the three different grid densities (coarse ($85 \times 120 \times 150$), fine ($95 \times 130 \times 160$), and finest ($105 \times 140 \times 170$)) for all the jet inlet conditions. The self-similar solution for each jet inlet condition is tested at the downstream location $x/h = 20$ in the lateral and wall-normal directions. From the Figure 3.16, it can be seen that the coarse grid density ($85\times120\times150$) and fine grid density ($95\times130\times160$) predict approximately similar self-similar velocity profiles in the lateral direction. The maximum deviation of the self-similar velocity profile between the coarser grid and the fine grid is 1.9%. Further, the finest grid density ($105 \times 140 \times 170$) is included to test the grid independence. The maximum deviation of the similarity parameter u/u_{max} is 0.01%. So, fine grid density is selected for all the numerical simulations. The value of $Y^+ \left(= U_\tau y/\vartheta\right) < 1.0$,

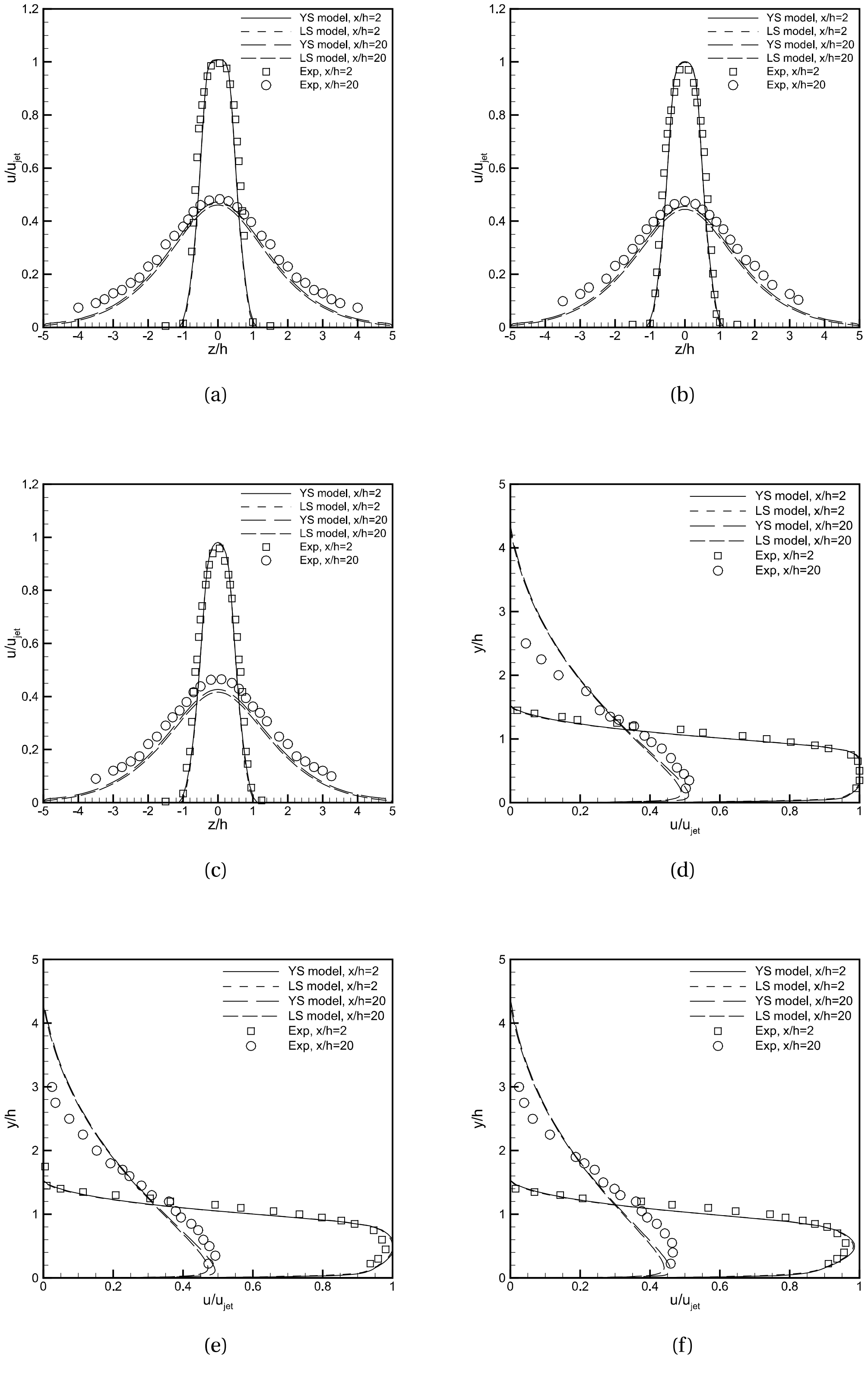

Figure 3.15: Code validation of the velocity profiles for YS and LS models in lateral direction for (a) $l/h = 10$, (b) $l/h = 50$, (c) $l/h = 90$, and in wall-normal direction for (d) $l/h = 10$, (e) $l/h = 50$, (f) $l/h = 90$

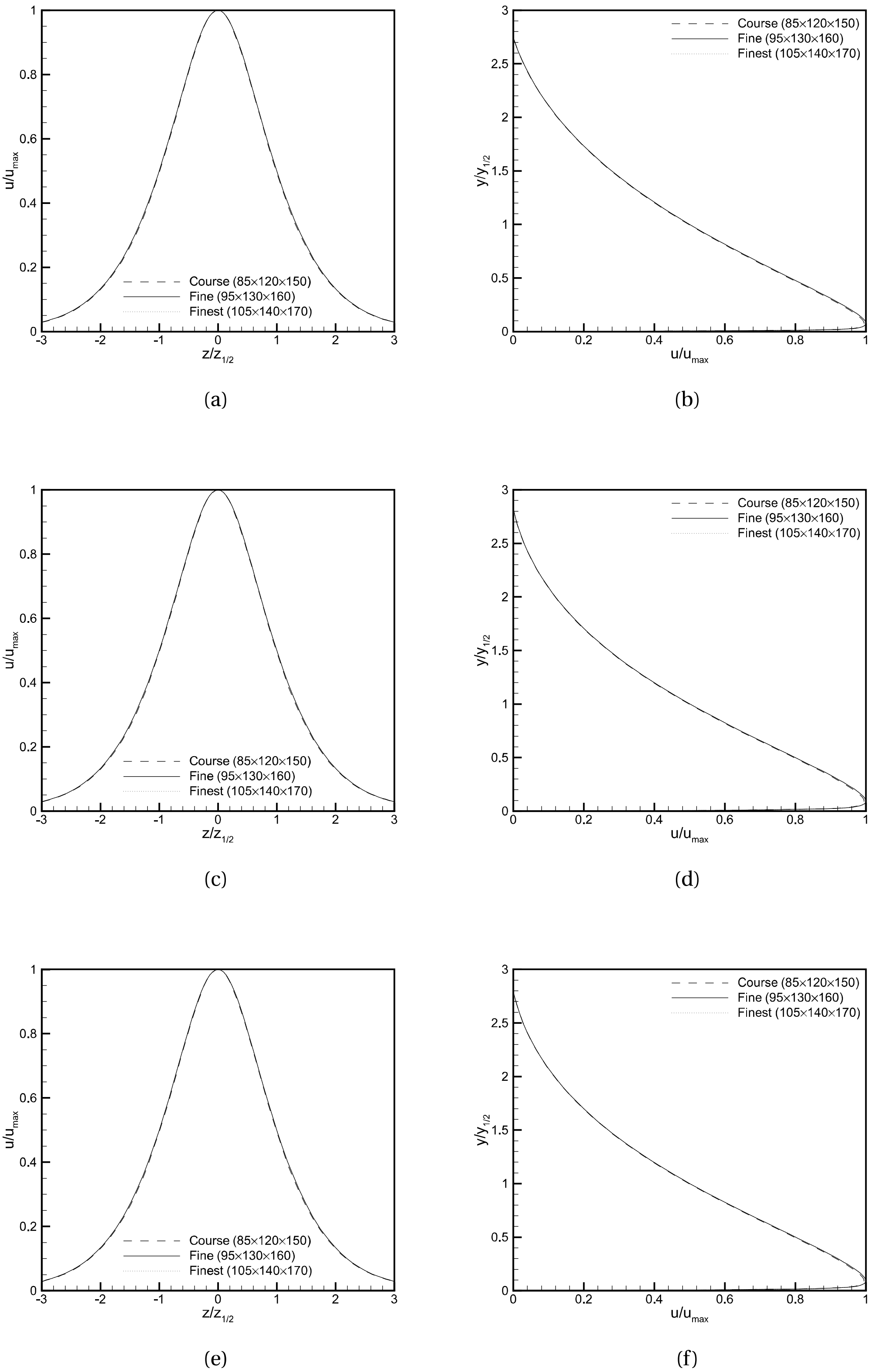

Figure 3.16: Grid independence test for different initial conditions of the jet

ensures that the first grid point is in the viscous sub-layer zone for each case. The value varies from 0.007 to 0.9 for the bottom wall of the wall jet.

3.2.6.2 Effect of sidewalls

The numerical code for heat transfer and fluid flow characteristics is validated with the experimental result in both the configurations (described in section 3.1.3.2) of the three-dimensional wall jet as shown in Figures 3.17, 3.18, 3.19 and 3.20. The numerical code is validated for the similarity solution (suggested by Wygnanski et al. [32]) for velocity and temperature fields. The numerical results are obtained with the $k-\epsilon$ low Reynolds number YS and LS turbulence models. From the Figure 3.18, it can be seen that the jet profile at the downstream location $x/h = 20$ is deviated from the experimental results in the upper shear layer. The maximum deviation from the experimental results is about 10% and 20% in configuration 1 and configuration 2 respectively. The deviation in three-dimensional wall jet from the experimental results is due to the differences in experimental conditions during the experimental run, possible presence of room drought at outer shear layers and used measurement techniques. A slight movement of surrounding fluid may affect the measurement. In the lateral edge and upper shear layer of the jet, the experimental measurement technique (intrusive measurement technique) may also be the reason for the deviation of the experimental and numerical results. The production of the turbulence in wall-normal shear layers at y_{max} is significantly low but the large production of the turbulence is present in the outer shear layer, which are large-scale structures transported to another location near the wall surface to dissipate [136, 137]. The production of the turbulence at the outer shear layers is dependent on the boundary conditions, which leads to increase or decrease in the production rate in the outer shear layer. The production of the turbulence indicates the mixing strength of the fluids inside the flow domain. This mixing of the flow is captured in the RANS simulation by using the gradient-diffusion hypothesis. In this hypothesis, the use of linear relation between Reynolds stresses with velocity gradient may also be the reason for the deviation between the experimental and numerical results of the highly anisotropic flow behaviour of the three-dimensional turbulent wall jets. The velocity profile in Figures 3.19 and 3.20 shows a quite good agreement with the experimental results for both the configurations. The deviation in velocity field occurs in the outer shear layer of the flow field in both the configurations. This may be due to the lower mixing in RANS model. From the flow field of the temperature and velocity, the local value of velocity and temperature computed by YS model is 5-6% more accurate (average) as compared to LS model.

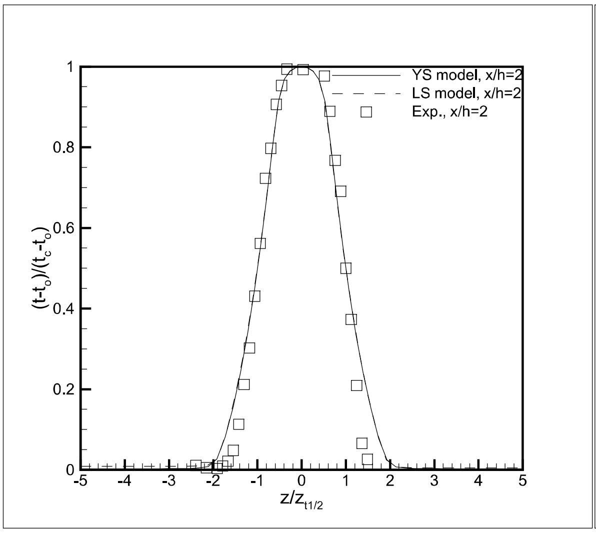

(a) Temperature validation in lateral direction for configuration 1 at $x/h = 2$

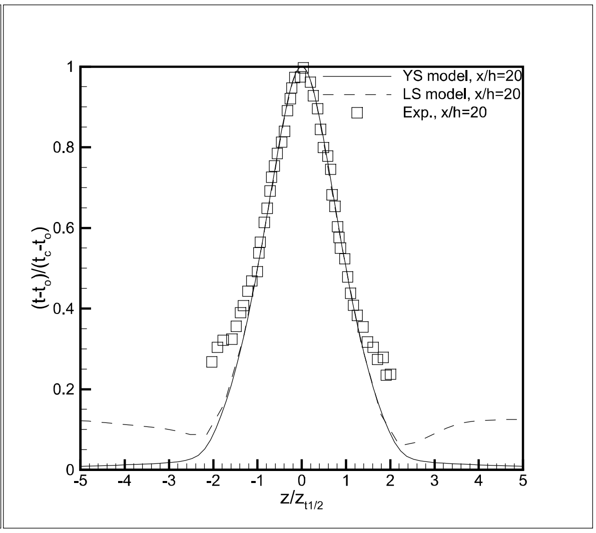

(b) Temperature validation in lateral direction for configuration 1 at $x/h = 20$

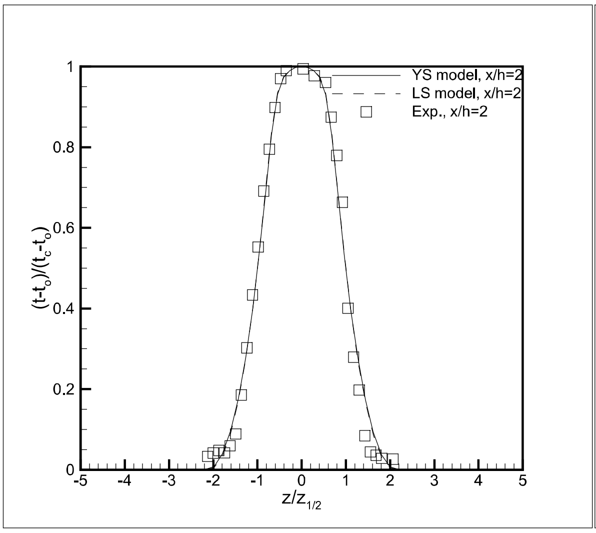

(c) Temperature validation in lateral direction for configuration 2 at $x/h = 2$

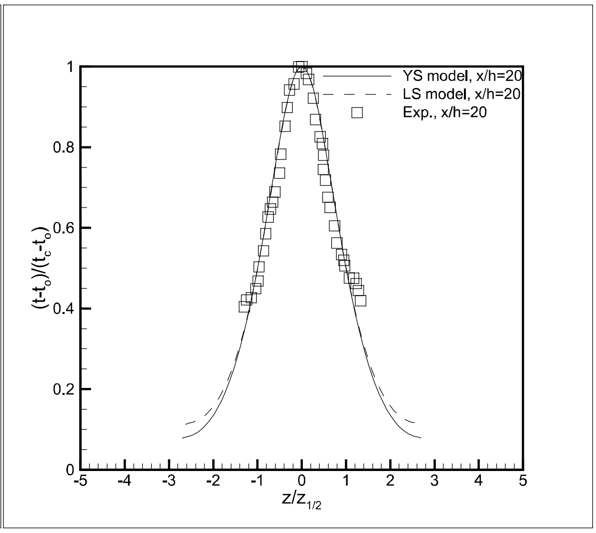

(d) Temperature validation in lateral direction for configuration 2 at $x/h = 20$

Figure 3.17: Temperature validation in lateral direction

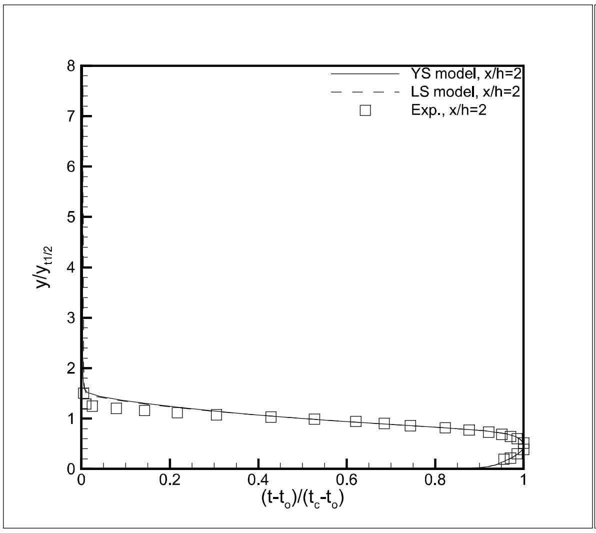

(a) Temperature validation in wall-normal direction for configuration 1 at $x/h = 2$

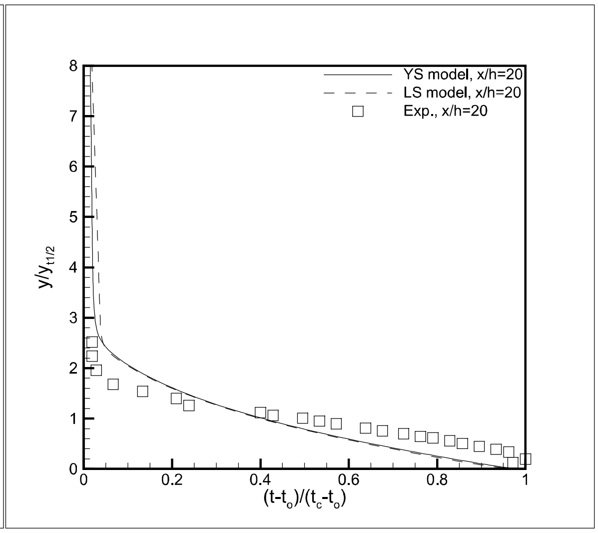

(b) Temperature validation in wall-normal direction for configuration 1 at $x/h = 20$

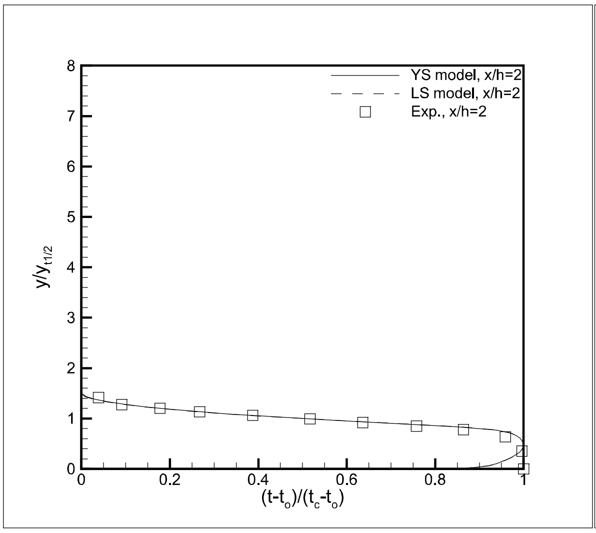

(c) Temperature validation in wall-normal direction for configuration 2 at $x/h = 2$

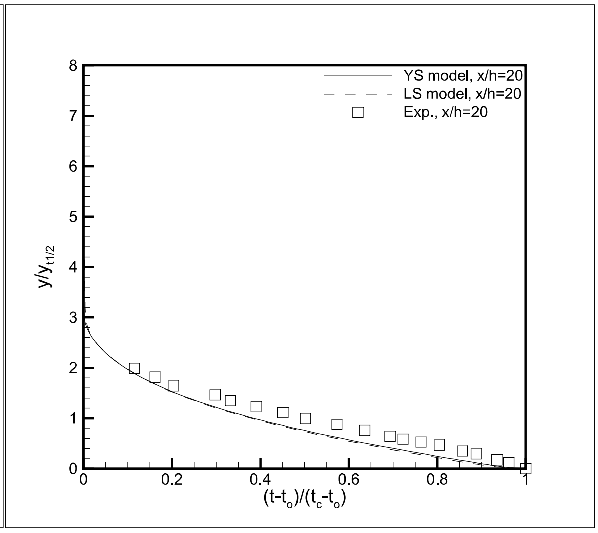

(d) Temperature validation in wall-normal direction for configuration 2 at $x/h = 20$

Figure 3.18: Temperature validation in wall-normal direction

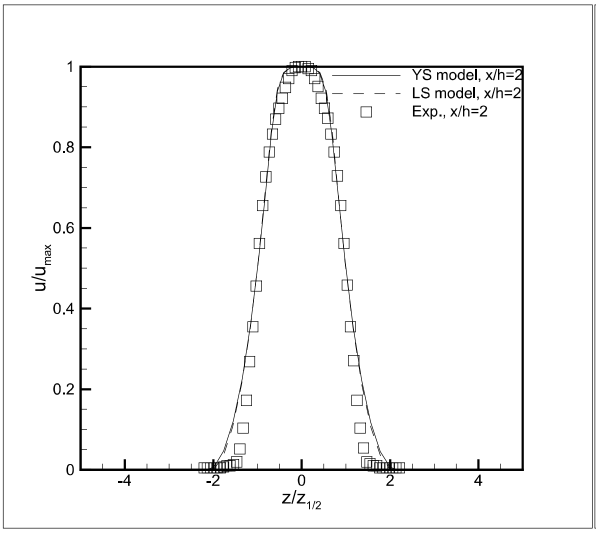

(a) Velocity validation in lateral direction for configuration 1 at $x/h = 2$

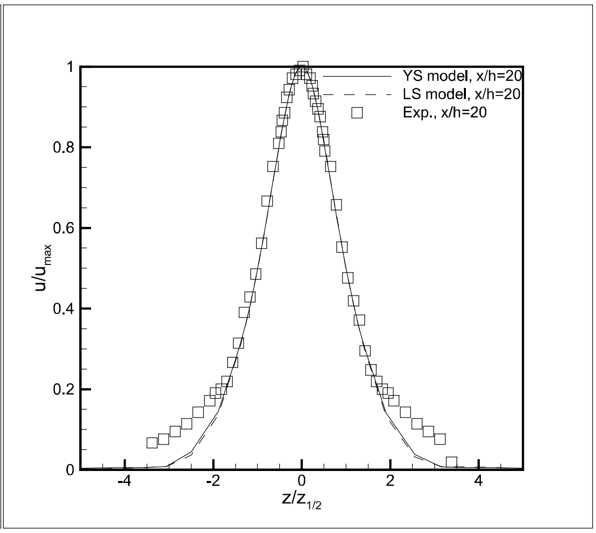

(b) Velocity validation in lateral direction for configuration 1 at $x/h = 20$

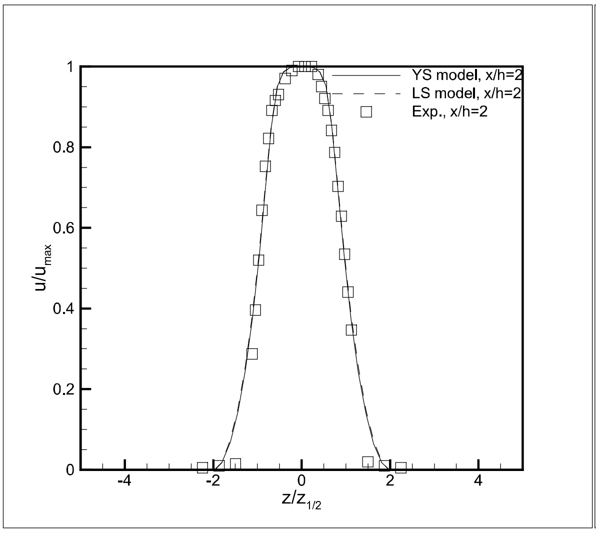

(c) Velocity validation in lateral direction for configuration 2 at $x/h = 2$

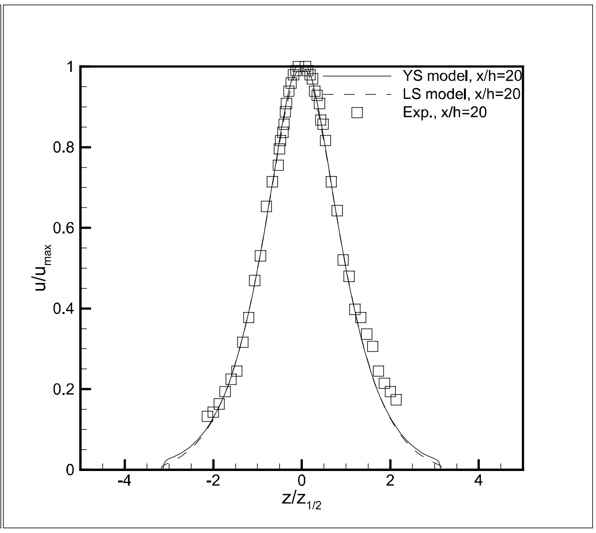

(d) Velocity validation in lateral direction for configuration 2 at $x/h = 20$

Figure 3.19: Velocity validation in lateral direction

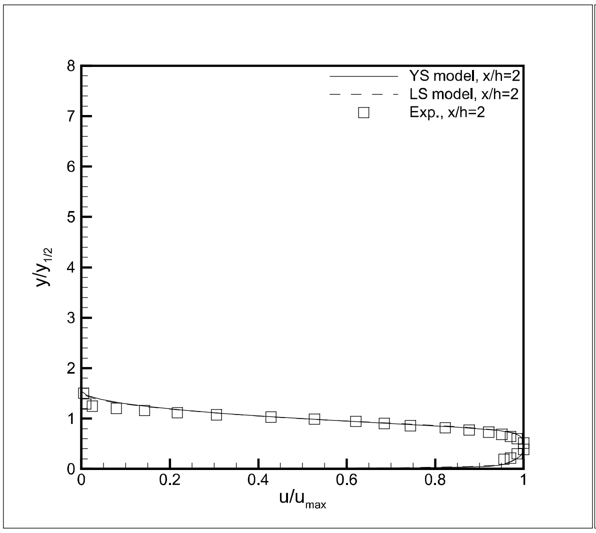

(a) Velocity validation in wall-normal direction for configuration 1 at $x/h = 2$

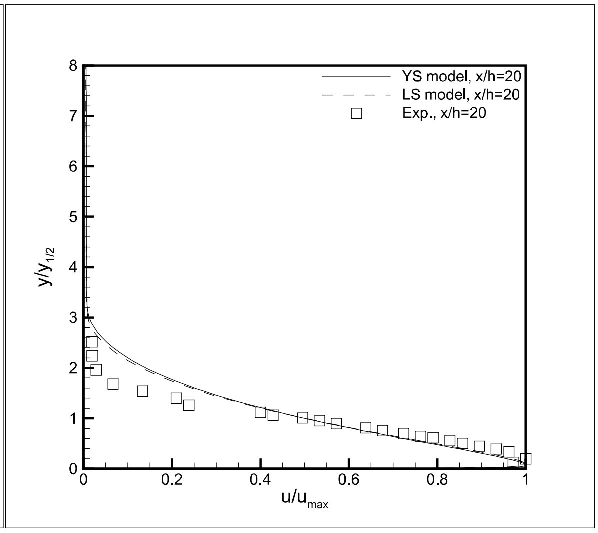

(b) Velocity validation in wall-normal direction for configuration 1 at $x/h = 20$

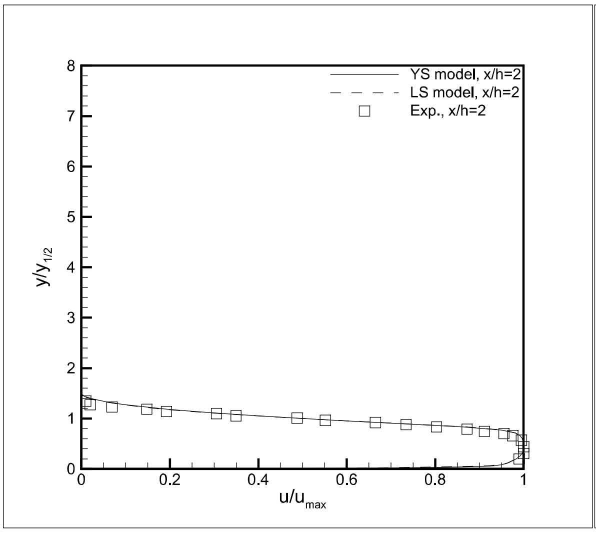

(c) Velocity validation in wall-normal direction for configuration 2 at $x/h = 2$

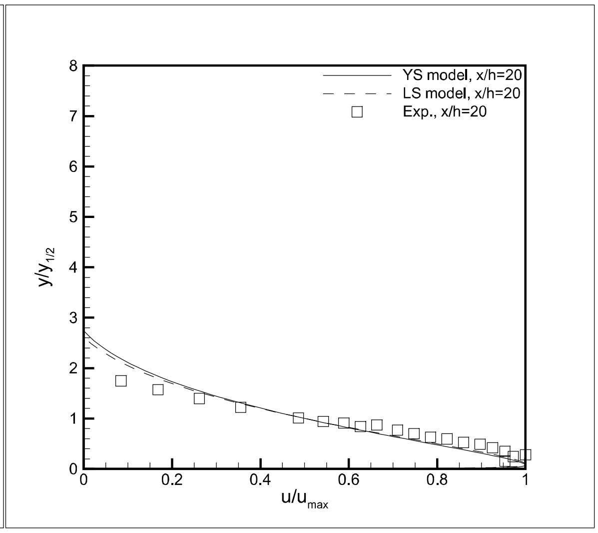

(d) Velocity validation in wall-normal direction for configuration 2 at $x/h = 20$

Figure 3.20: Velocity validation in wall-normal direction

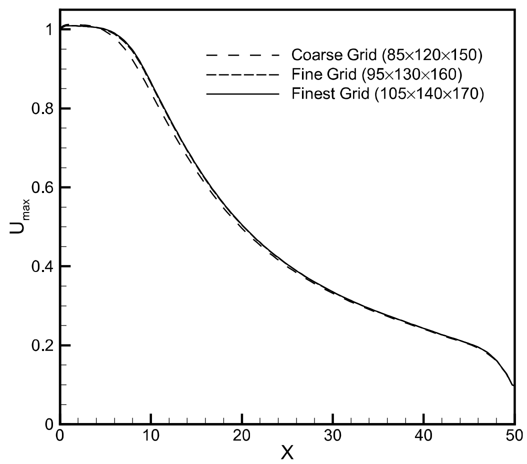

Figure 3.21: Variation of decay of normalized maximum mean velocity for different grid densities

Before proceeding with the productive run, grid independence test was carried out. Since decay of normalized maximum mean velocity (U_{max}) is one of the important parameters in turbulent wall jet, it is selected for the grid independency test. A high grid density is considered near the bottom wall and jet exit region. It has been ensured that the first grid point near the wall lies near the viscous sub layer zone $\left(Y^+ \left(= U_\tau y/\vartheta\right) < 1.0\right)$. The value of Y^+ for the first grid point varies in the range of $0.007 \le Y^+ \le 0.9$ for the bottom wall. Figure 3.21 shows the variation of normalized maximum mean velocity for different grid densities for a sidewall spacing of $10h$. Three sets of grid are chosen for the test; they are: coarse (85 × 120 × 150), fine (95 × 130 × 160), and finest (105 × 140 × 170). It is noticed that the coarse grid gives almost similar result to the other two grids except in the region where jet interacts with the sidewall. But, upon further refinement in grid density, the results almost converge for fine and finest grid sets. Therefore, a grid density of 95 × 130 × 160 is selected for entire study with a sidewall spacing of $10h$.

3.2.6.3 Effect of sidewall enclosure width

The numerical code is validated by the experimental results of $140mm$, $160mm$, $180mm$ and $200mm$ SWEs at the Reynolds number of 25,000. The numerical results are obtained with the low Reynolds number YS and LS turbulence models. The streamwise velocity component (u) are compared at the downstream locations $x/h = 2$ and 20 in lateral and wall-normal directions for all the SWE cases. From Figure 3.22, it can be seen that the variation of the u velocity profile shows quite a good match with the experimental results for

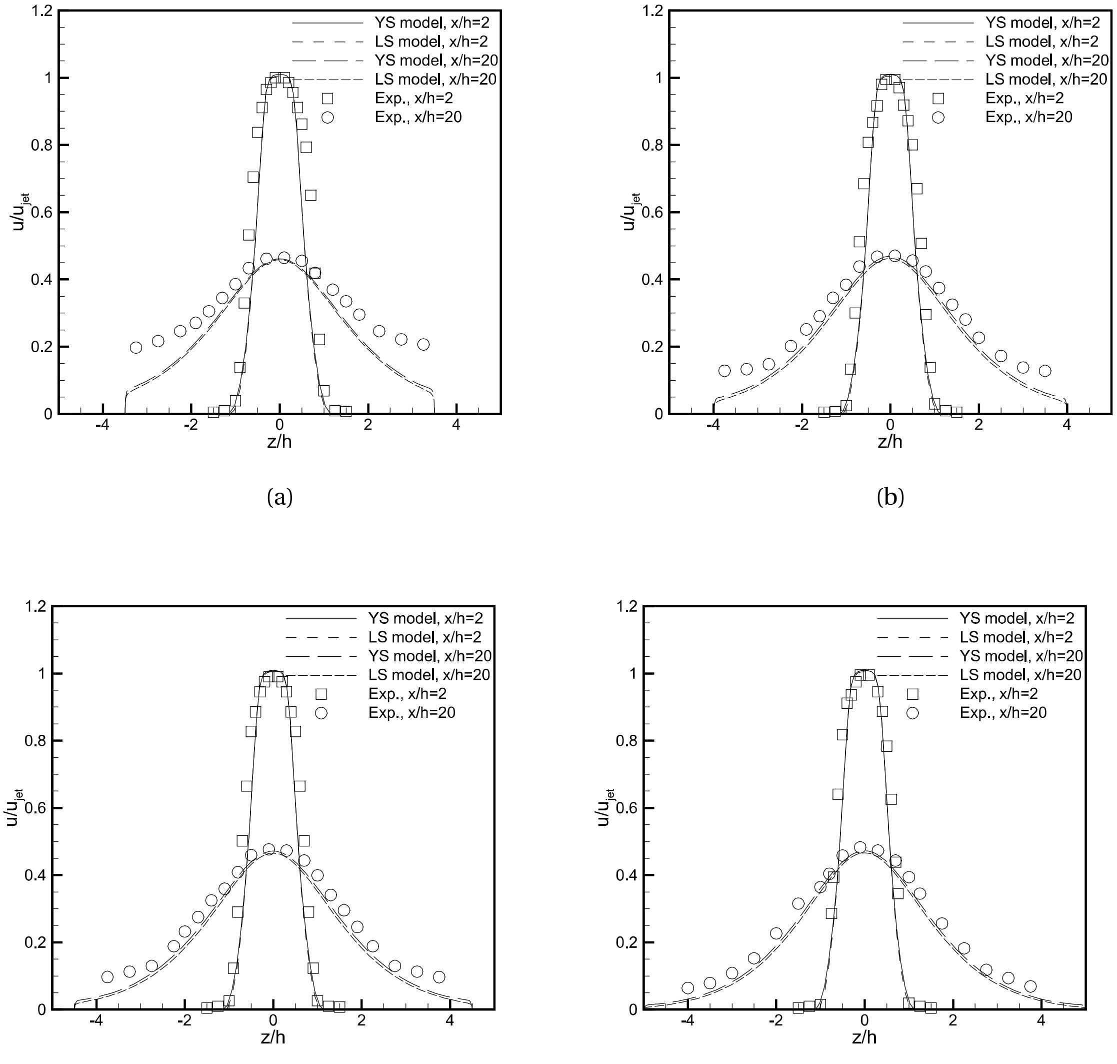

(a) (b)

(c) (d)

Figure 3.22: Code validation of the velocity distribution for (a) 140mm SWE in lateral direction, (b) 160mm SWE in lateral direction, (c) 180mm SWE in lateral direction and (d) 200mm SWE in lateral direction

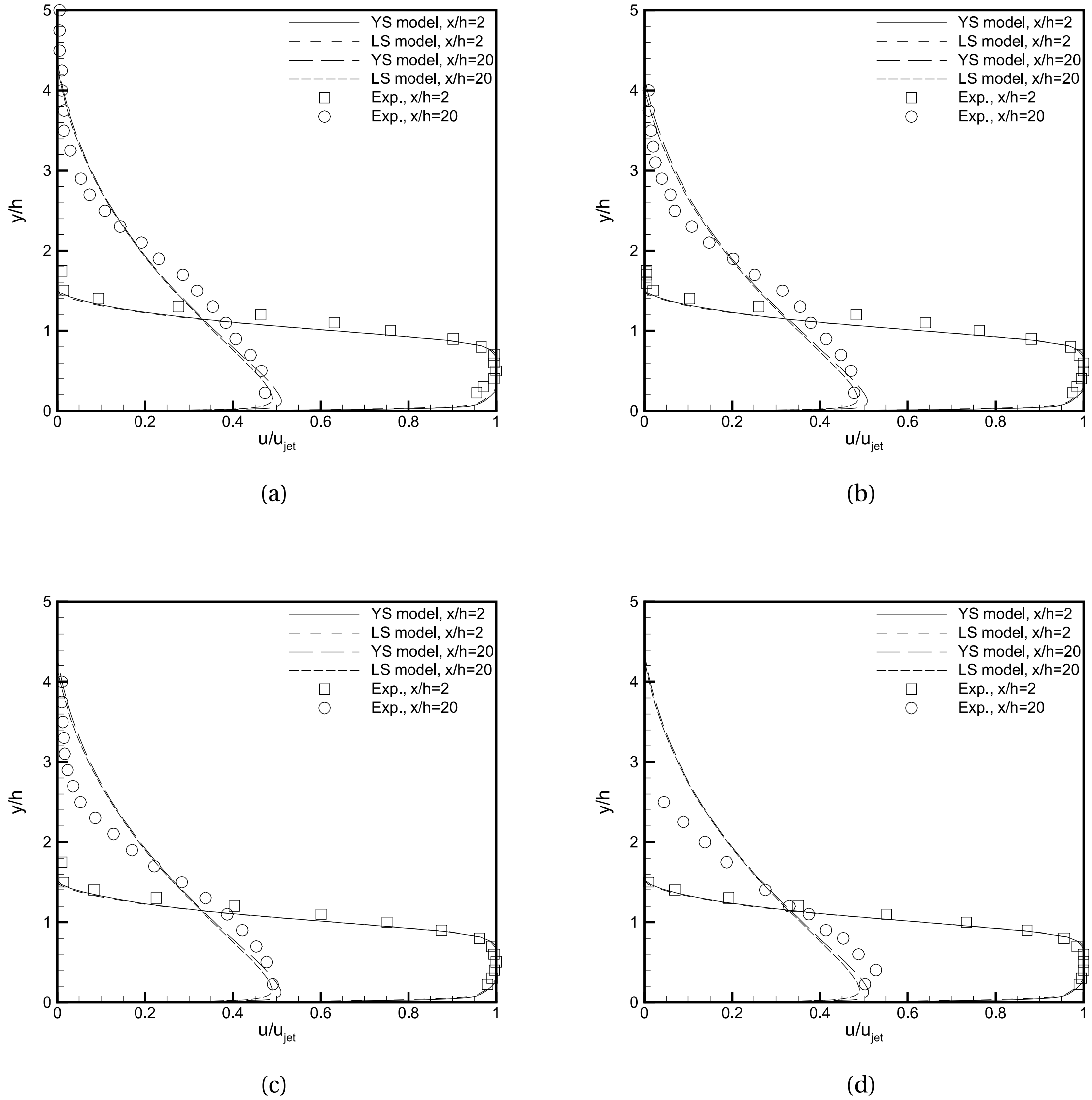

Figure 3.23: Code validation of the velocity distribution for (a) 140mm SWE in wall-normal direction, (b) 160mm SWE in wall-normal direction, (c) 180mm SWE in wall-normal direction and (d) 200mm SWE in wall-normal direction

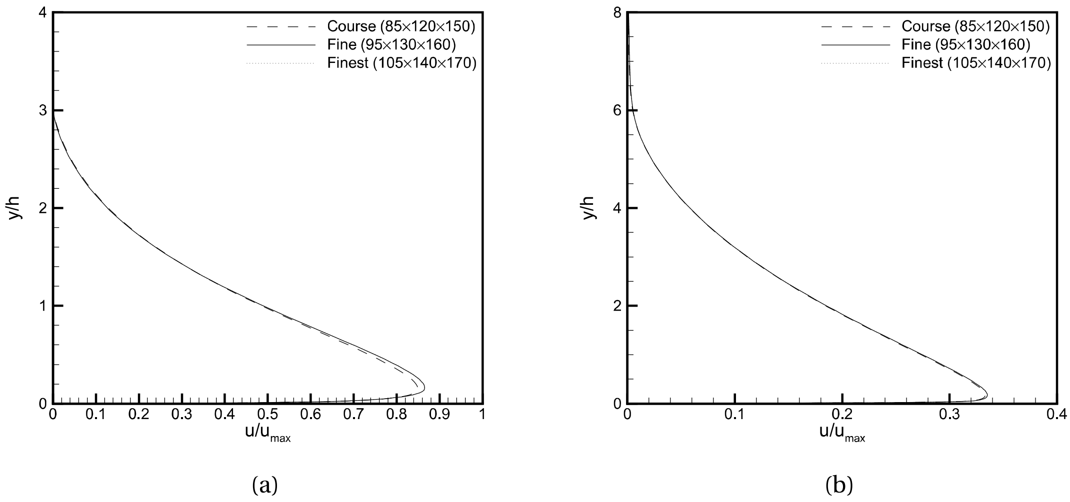

Figure 3.24: Variation of the wall-normal velocity at (a) $x/h = 10$, and (b) $x/h = 30$ for different grid density as described in labels

all the SWEs. The deviation in velocity field occurs at the outer shear layer of the flow field in all SWEs, and it increases with decrease in the width of the SWE due to the anisotropic behaviour of the sidewalls. The deviation may also be attributed to the invasive measurement techniques used in the present work. The smaller width of SWE leads to a higher disturbance, resulting in a higher deviation.

The grid independence test for 200mm SWE is presented in Figure 3.24. It represents the variation of a wall-normal velocity profile for the different tested grid densities. Three grid densities are chosen as coarse ($85 \times 120 \times 150$), fine ($95 \times 130 \times 160$), and finest ($105 \times 140 \times 170$). From Figure 3.24, it can be observed that the coarser grid density predicts similar results of the wall-normal velocity profile at $x/h = 10$ and $x/h = 30$. The predicted value of u_{max} at $x/h = 10$ of the coarser grid deviates approximately 1.85% from the fine grid. Further, the finest grid density ($105 \times 140 \times 170$) is also tested, and a negligible difference in the value of u_{max} is obtained between the fine grid density ($95 \times 130 \times 160$) and the finest grid density ($105 \times 140 \times 170$). So, for the present numerical simulation of the enclosure width $10h$, fine grid density ($95 \times 130 \times 160$) is chosen. The grid independence test is performed for all the sidewall enclosures. The grid independence test is carried out for each set of SWE. The grid density size for the enclosure width $7h$, $8h$, $9h$ and $10h$ is $81 \times 126 \times 160$, $87 \times 130 \times 160$, $91 \times 130 \times 160$ and $95 \times 130 \times 160$, respectively. The grid densities are kept higher near the wall surfaces and nozzle inlet. The first grid point near the wall surfaces is kept in the viscous sub-layer region where $Y^+ < 1$ for all the SWEs.